ROYAL SOCIETY OF CHEMISTRY

www.rsc.org/pccp

Near-infrared down-conversion and energy transfer mechanism in Yb^{3+}-doped $Ba_2LaV_3O_{11}$ phosphors

Jin Zhao[1], Chongfeng Guo[1*], Ting Li[1], Dan Song[1], Xiangying Su[2]

[1]*National Key Laboratory of Photoelectric Technology and Functional Materials (Culture Base) in Shaanxi Province, National Photoelectric Technology and Functional Materials & Application of Science and Technology International Cooperation Base, Institute of Photonics & Photon-Technology, Northwest University, Xi'an 710069, China*

[2]*School of Physics & Engineering, Henan University of Science &Technology, Luoyang, 471023, China*

---

* Author to whom correspondence should be addressed

Tel. & Fax.: 86-29-88302661

E-mail: guocf@nwu.edu.cn (Prof. Guo)

Abstract

Yb^{3+}-doped $Ba_2LaV_3O_{11}$ vanadate phosphors with near infrared (NIR) emission are synthesized via the sol-gel method. The phase purity and structure of samples are characterized by X-ray diffraction (XRD). The electronic structure of self-activated phosphor host $Ba_2LaV_3O_{11}$ is estimated by density functional theory (DFT) calculation, and the host absorption is mainly ascribed to the charge transition from the O-2*p* to V-3*d* states. Photoluminescence emission (PL) and excitation (PLE) spectra, decay curves, absorption spectra and theoretical quantum yields of samples are also investigated. It indicates that $Ba_2LaV_3O_{11}$: Yb^{3+} phosphors have strong broad band absorption and efficient NIR emission, which matches well with the spectral response of the Si-based solar cells. The energy transfer processes from $[VO_4]^{3-}$ to Yb^{3+} and possible transfer models are proposed on the concentration of Yb^{3+} ions. Results demonstrate that $Ba_2LaV_3O_{11}$: Yb^{3+} phosphors might act as promising NIR DC solar spectral converter to enhance efficiency of the silicon solar cells by utilizing the broadband absorption for solar spectrum.

Keywords: Phosphor; Energy transfer; Vanadates; Near-infrared Down-conversion.

1. Introduction

Solar energy is an inexhaustible renewable green energy and expected to provide about 16% of the entire global electricity by the year 2050, leading to the rapid growth of the solar energy application and research in recent years.[1, 2] Photovoltaic cells could convert solar energy directly into electricity, which has aroused more interests of many governments, large-scale enterprises and experts to develop. Among various solar cells, crystalline silicon (c-Si) solar cells still dominate the commercial market though its photo-electric conversion efficiency is far below the theoretical maximum value 30% (the Schockley-Queisser limit) due to the spectral mismatch between sunlight spectrum (300-2500 nm, AM 1.5G) and the response curve of c-Si semiconductor ($E_g \approx 1.12$ eV, $\lambda \approx 1100$ nm).[3, 4] In general, the spectral response of conventional Si-based solar cells (as shown in Fig. 8) is much weaker in ultraviolet region below 400 nm, and the much higher energy than E_g of ultraviolet-visible (UV-Vis) photons will lose as heat during the fast thermalization of hot charge carriers. Moreover, the low energy photons ($E < E_g$) at infrared region cannot be absorbed.[5] To reduce the spectral mismatch losses and enhance the efficiency of silicon solar cells, down-conversion (DC) phosphors including down-shift (DS) and quantum cutting (QC) modes based on the energy transfer process have been put forward to put in the front of the solar cells to modify the incident spectrum, which could provide a promising way for the improvement of solar cell efficiency by convert inefficient UV-visible short-wavelength light to available near-infrared (NIR) photons close to E_g.[6-8]

Recently, investigations of the NIR DC materials were mainly focused on the RE^{3+}-Yb^{3+} (RE = Tb^{3+}, Pr^{3+}, Tm^{3+}, Ho^{3+}, Er^{3+} or Nd^{3+}) or Ce^{3+} / Eu^{2+}-Yb^{3+} co-doped phosphors, in which RE^{3+} or Ce^{3+} / Eu^{2+} ions act as sensitizers to UV-Vis and transfer their energy to Yb^{3+} to produce near infrared emission. However, the former typical narrowband donors (*e.g.* Tb^{3+}) suffer from naturally weak and narrow absorption cross-section in the UV / blue region because of the partially forbidden 4*f*-4*f* transitions;[9-12] the latter broadband absorption ions (Ce^{3+}, Eu^{2+}) from the allowed 4*f*-5*d* transitions have to be produced in reducing atmosphere and easy to produce reduction state like Yb^{2+},[13, 14] leading to weak NIR emission. In these systems, Yb^{3+} ion is used as proper acceptor and efficient NIR emitting center at around 1000 nm assigned to simple $^2F_{5/2} \rightarrow {}^2F_{7/2}$ transition, which is in agreement with the optimal spectral response of c-Si.[15] Yb^{3+}-doped host-sensitized NIR DC luminescent materials (*e.g.* VO_4^{3-}, NbO_4^{3-}, WO_4^{2-} and MoO_6^{6-} group contained host matrices) like YVO_4, $CaLaNb_3O_{10}$ could not only avoid the above drawbacks but also offer excellent physical and chemical stability, strong absorption in the UV range and intense emission in the Vis / NIR region, efficient energy transfer (ET) from the host to the doping Yb^{3+} ions, which satisfy the requirements for phosphors in the application of silicon solar cells.[16-19] As a self-activating material, most vanadates possess broad and strong excitation band from n-UV to visible region as well as broad emission covering from blue to red due to their charge transfer (CT) transitions in the $[VO_4]^{3-}$ group.

In this work, monoclinic structure $Ba_2LaV_3O_{11}$ is selected to accommodate Yb^{3+} ions and to investigate their NIR emission properties under UV light. The structure, visible and NIR emission spectra and decay curves are investigated to prove the existence of ET from $[VO_4]^{3-}$ to Yb^{3+}. ET mechanisms are systematically studied and discussed. Results indicate that the current $Ba_2LaV_3O_{11}$: Yb^{3+} NIR DC phosphor have potential application to modify the solar spectrum and enhance the conventional efficiency of silicon solar cells.

2. Experimental

2.1 Preparation of phosphors

The $Ba_2LaV_3O_{11}$: xYb^{3+} (x = 0, 0.01, 0.04, 0.08, 0.16, 0.20, 0.30) powers are synthesized via sol-gel method. At the beginning, the stoichiometric amounts of raw materials, including high purity La_2O_3, Yb_2O_3 (99.99%, Shanghai Yuelong Nonferrous Metals Ltd.) and analytical reagents (A.R) $BaCO_3$, NH_4VO_3 and citric acid are weighted, respectively. First, rare earth oxides and $BaCO_3$ are dissolved in nitric acid HNO_3 (AR) with heating and stirring, and the redundant HNO_3 is dried out by heating and evaporation. Afterward, a certain amount of de-ionized water is added to form transparent solution. Then, NH_4VO_3 and chelating agent citric acid for the metal ions are added in succession, and the molar ratio of total chelate metal cations to citric acid is fixed at 1: 2. At the end, the pH value of the mixture is adjusted to 1 by adding diluted HNO_3, with constant stirring until highly transparent green-yellow precursor solution is obtained. Then obtained solutions are heated at 70 ℃ for 48 h in an oven to get black resins, further dried at 120 ℃ for 24 h to form foam black dried gel. Finally, the dried gels are pre-heated in air at 500 ℃ for 5 h, reground, and then calcined at 1000 ℃ for 5 h to get final product.

2.2 Characterization of phosphors

The powder X-ray diffraction (XRD) of samples are carried out by using a Rigaku-Dmax 3C powder diffractometer (Rigaku Corp, Tokyo, Japan) at 40 kV, 30 mA with Cu-Kαasan incident radiation (λ = 1.54065 Å). Diffuse reflection spectra (DRS) are taken on a VARIAN CARY 5000 UV-Vis-NIR spectrophotometer with a reference $BaSO_4$ powder. The PL excitation and emission spectra and decay curves are recorded on an Edinburgh FLS920 spectrometer equipped with a 450 W Xe lamp and combined μF900 microsecond flash-lamp as excitation sources. PL spectra of all samples are tested more than three times to reduce the error and all of the measurements are performed at room temperature.

2.3 Computational procedure

Our calculations are performed using the VASP 5.2 program, in which the first principles wave-basis pseudo-potential method is used within the density functional theory (DFT).[20, 21] Projector-augmented-wave (PAW) potentials are adapted for Ba, La, V and O atoms, while generalized gradient approximation (GGA) under the scheme of Perdew-Burke-Ernzerhof (PBE) functional is used for the electron exchange-correlation interactions.[22] A plane-wave basis set with an energy cutoff of 400 eV is employed. Self-consistency is considered to be achieved when the total energy difference between succeeding iterations is less than 10^{-5} eV. A k-point sampling of 1×3×5 Monkhorst-Pack mesh is used for the relaxation calculations and a 3×10×15 mesh is applied for the calculations of DOS.

3. Results and discussion

3.1. X-ray diffraction and structural characterization

It is well known that the structure determines the property of materials, thus it is necessary to identify the structure of samples. The XRD patterns of the as-synthesized $Ba_2LaV_3O_{11}$: xYb^{3+} samples are used to characterize the structure of sample and shown in Fig. 1a as a function of Yb^{3+} doping concentrations. It is found that all the XRD patterns are similar and match well with the standard data of $Ba_2BiV_3O_{11}$ (JCPDS No.81-1778), no any purity diffraction peaks appeared with the introduction of Yb^{3+}. This indicates that $Ba_2LaV_3O_{11}$ and $Ba_2BiV_3O_{11}$ are iso-structural and adopt the same monoclinic structure, and the introduction of Yb^{3+} does not cause any changes of structure. However, it is observed that the diffraction peaks gradually shift toward higher angles with the increase doping of Yb^{3+} ions and variable trend of main peak (021) is shown in Fig. 1b, which due to the replacement of La^{3+} (R_{La} = 1.03 Å for CN = 6) by Yb^{3+} ions with smaller ionic radius (R_{Yb}= 0.87 Å, CN = 6).

$Ba_2LaV_3O_{11}$ and $Ba_2BiV_3O_{11}$ with the general formula $Ba_2MV_3O_{11}$ (M=Bi, In, or rare earth) crystallize in the monoclinic system with the space group *P21/a*, which contains both an orthovanadate group $[VO_4]^{3-}$ and a pyrovanadate group $[V_2O_7]^{4-}$. *$[V_2O_7]^{4-}$ is formed by two $[VO_4]^{3-}$ groups sharing one oxygen atom, and* the V^{5+} ions in $[VO_4]^{3-}$ and $[V_2O_7]^{4-}$ groups are tetrahedrally surrounded via connecting four oxygen atoms, the formula of $Ba_2MV_3O_{11}$ can be rewritten as $Ba_2M(VO_4)(V_2O_7)$. [23] Figure 1c displays the sketch of the contents of a $Ba_2MV_3O_{11}$ *unit cell. It* is observed that the M^{3+} atom coordinates to six oxygen atoms forming a distorted octahedron and there are two types of Ba atoms with coordination numbers of 11 (Ba1) and 10 (Ba2). The calculated cell parameters of $Ba_2LaV_3O_{11}$ are a = 24.63 Å, b = 7.77 Å, c =5.55 Å and V= 1034.24 $Å^3$, are close to those of $Ba_2BiV_3O_{11}$ (a = 24.65 Å, b = 7.73 Å, c = 5.64 Å and V= 1046.50 $Å^3$, JCPDS 81-1778) due to the tiny difference of ionic radii between R_{La} = 1.032 Å and R_{Bi} = 1.030 Å for CN = 6. [24]

3.2. Electronic structure and diffuse absorption spectra of $Ba_2LaV_3O_{11}$ host

The electronic structure of $Ba_2LaV_3O_{11}$ is investigated by first principle calculation using VASP code, and the calculated band structure of host compound is expressed in Fig. 2a. The results display that the pure $Ba_2LaV_3O_{11}$ has a direct band-gap of 3.09 eV because the valence bands maximum (VBM) and the conduction bands minimum (CBM) located at the same point. It can be concluded that the $Ba_2LaV_3O_{11}$ is a suitable host for luminescence materials with a wide band gap between 3.0 and 6.0 eV because it helps to accommodate both the ground and excited states of luminescent ions within the band gap.[25] In order to understand the composition of the energy bands, the total and partial density of states (DOS) of $Ba_2LaV_3O_{11}$ are calculated (see Fig. 2b). It is clearly observed that the top of valence band is composed of dominant O-2p and there is a small contribution from the V-3d, 3p, 4s and La-5d states ranging from -5 eV to the Fermi level (set at 0 eV). Another band between -8 eV and -20 eV is created by Ba-5p, La-6p, V-3d, 3p, 4s and O-2s states, while the bottom of conduction band in $Ba_2LaV_3O_{11}$ ranging from 3.09 eV to 7.60 eV is mainly formed by V-3d states and a slight contribution of the O-2p. Results provide useful information about the host lattice, which displays that host absorptions can be mainly ascribed to the charge transition (CT) from the O-2*p* to V-3*d* states.

The UV-visible diffuse reflectance spectrum of pure $Ba_2LaV_3O_{11}$ is depicted in Fig. 3a. The strong absorption band below 400 nm of the spectrum is ascribed to the host absorption, which may primarily ascribe to the transitions from O^{2-} to different levels of V^{5+} in tetrahedral $[VO_4]^{3-}$ group. The optical band gap energy E_g can be calculated by the method based on the transformation of diffuse reflectance measurements put forward by Kubelka and Munk. The Kubelka–Munk function $F(R_\infty)$ is defined as: [26]

$$F(R_\infty) = (1-R)^2/2R = K/S \qquad (1)$$

where R, K and S are the reflection, the absorption and the scattering coefficient, respectively. The modified Kubelka-Munk equation gained as follow: [27]

$$[F(R_\infty)h\nu]^n = A(h\nu - E_g) \qquad (2)$$

here $h\upsilon$ is the photon energy, A is a proportional constant, E_g is the value of the band gap, n=2 for a direct transition or 1/2 for an indirect transition. From the linear extrapolation of $[F(R_\infty)h\upsilon]^2=0$, the band gap of as-synthesized $Ba_2LaV_3O_{11}$ is calculated to be 3.35 eV as shown in Fig. 3b. However, the experiment value is higher than the theoretical calculated value (3.09 eV) due to GGA potential usually underestimates the size of the band gap. [28]

3.3 Analysis of photoluminescence spectra and energy transfer processes

3.3.1 Luminescent properties of self-activated $Ba_2LaV_3O_{11}$ phosphor

Photoluminescence excitation (PLE) and emission (PL) spectra of the un-doped $Ba_2LaV_3O_{11}$ at room temperature are presented in Fig. 4a. According to the electronic structure calculation results, the broad band emission is attributed to charge transfer of an electron from the 2*p* orbital of the oxygen atom (O-2*p*) to the vacant 3*d* orbital of V^{5+} ions (V-3*d*) in tetrahedral $[VO_4]^{3-}$ group with T_d symmetry. In order to better understand the assignment of the spectra, schematic energy levels for the possible excitation and emission transitions in VO_4 tetrahedron are shown in Fig. 4b. Typically, the molecular orbitals of the V^{5+} ion with T_d symmetry are expressed as a ground state $^1A_1$ and four excited states $^1T_1$, $^1T_2$, $^3T_1$, and $^3T_2$, and the energy separation between $^3T_1$ and $^3T_2$ is about 2000 cm^{-1}.[29] Monitoring at about 502 nm, $Ba_2LaV_3O_{11}$ exhibits a broad excitation band between 240 and 395 nm centered at 338 nm. According to the Gaussian analysis, the excitation band can be decomposed to two absorption bands peaking at about 312 and 344 nm, which are assigned to the partly enabled spin-allowed transitions from the ground state to the excited state $^1T_2$ and $^1T_1$ transitions, respectively. Regarding the two absorption bands in the PLE spectrum, the minor intensity band corresponding to the $^1A_1\rightarrow{}^1T_2$ (Ex$_1$) transition is known as a shoulder peak; and the major intensity is due to the $^1A_1\rightarrow{}^1T_1$ (Ex$_2$) transition. The intensities and positions of the two excitation bands Ex$_1$ and Ex$_2$ may depend on two factors: the concentration of the $[VO_4]^{3-}$ groups and the nature of the host lattice.[30] From the PL spectrum with the excitation of 338 nm, it is clear that phosphor exhibits the characteristic broad band emission ranging from 400 and 700 nm in yellow-green region with band maxima at 502 nm. It is well known that the asymmetric emission band of the vanadate contains two broad band peaks with maxima at 495 nm and 550 nm corresponding to the $^3T_2\rightarrow{}^1A_1$ (Em$_1$) and $^3T_1\rightarrow{}^1A_1$ (Em$_2$) spin-forbidden transitions of $[VO_4]^{3-}$ group, respectively. The de-convolved two emission bands are overlapped and they look like a single band with the naked eye because of the insignificant energy difference (about 0.2 eV) between the $^3T_1$ and $^3T_2$ excited states. To observe the difference between the two transitions, the emission spectrum is de-convolved into two bands using Gaussian fittings and the Em$_1$ band centered at 495 nm is more intense than that of the Em$_2$ band at 550 nm, as shown in Fig. 4a. These illuminate that $Ba_2LaV_3O_{11}$ could easily absorb high energy photons in the range of 240-400 nm and emit photons with lower energy in the visible region, which could be used to enhance the efficiency of Si-based solar cells without more heat dissipation.

3.3.2 Luminescence and ET in NIR DC $Ba_2LaV_3O_{11}$: Yb^{3+} phosphors

According to above results, it indicates that the emission of $[VO_4]^{3-}$ group could sensitize Yb^{3+}, and the PL and PLE spectra of samples $Ba_2LaV_3O_{11}$: $x$$Yb^{3+}$ as a function of Yb^{3+} contents *are* displayed in Fig. 5. The PLE spectra of sample with or without doping Yb^{3+} include a broad intense absorption band ascribed to the CT band involving $[VO_4]^{3-}$ groups rather than that of O^{2-}-Yb^{3+} which usually located at a wavelength shorter than 250 nm in inorganic compounds.[18] In addition, the profiles of PLE spectra for samples $Ba_2LaV_3O_{11}$: Yb^{3+} are similar except relative intensity as monitoring the $[VO_4]^{3-}$ emission at 502 nm and the $^2F_{5/2}\rightarrow{}^2F_{7/2}$ transition of Yb^{3+} at 1004 nm are shown in Fig. 5a, which indicates the energy transfer occurred from host to Yb^{3+}. Under the excitation of 338 nm, the PL spectra of Yb^{3+}-doped $Ba_2LaV_3O_{11}$ samples consists of a strong yellow-green emission at around 502 nm from the $[VO_4]^{3-}$ emission and an intense NIR emission with several weak shoulders peaking at 977, 995, 1004, 1069 nm from transitions among the different stark levels of ^2F_J (J=5/2, 7/2) of Yb^{3+} (as shown in Fig. 5b),[31] which also prove the existence of ET from host to Yb^{3+}. Seen from Fig. 5c, it is observed that the PL intensity of $[VO_4]^{3-}$ host intrinsic emission depresses monotonously with increased Yb^{3+} concentration from 0 to 0.3, whereas the NIR emission intensity firstly increases and then decreases after reaching the maximum at x=0.16 due to the concentration quenching effect.

Above results indicate that energy transfer plays an important role for the NIR emission in the Yb^{3+}-doped $Ba_2LaV_3O_{11}$ systems. To further confirm the ET existence from $[VO_4]^{3-}$ group to Yb^{3+}, the decay curves of $[VO_4]^{3-}$ group emission at 502 nm in $Ba_2LaV_3O_{11}$: $x$$Yb^{3+}$ system *are* plotted with variable Yb^{3+} concentrations upon 338 nm excitation are shown in Fig. 5d. The average lifetime (τ) of $[VO_4]^{3-}$ group in $Ba_2LaV_3O_{11}$: Yb^{3+} samples could be calculated by: [32]

$$\tau = \int_0^\infty tI_{(t)}dt \Big/ \int_0^\infty I_{(t)}dt \tag{3}$$

Where $I_{(t)}$ is the luminescence intensity at time t. The decay time of $Ba_2LaV_3O_{11}$ host is about 6.13 μs. With the introduction of Yb^{3+} ions, the decay curves significantly deviate from the single exponential rule and the decay rate of $[VO_4]^{3-}$ becomes faster with the increase of Yb^{3+} dosage. The energy transfer efficiency (ETE, η_{ETE}) from $[VO_4]^{3-}$ group to Yb^{3+} could be described as:[33]

$$\eta_{ETE} = 1 - \tau_x / \tau_0 \tag{4}$$

In which τ_x and τ_0 denote the decay life time of $[VO_4]^{3-}$ emission with and without Yb^{3+} doping. As the calculated values shown in Table 1, the average decay times of $[VO_4]^{3-}$ group diminish and the ETE rises correspondingly with the increase of Yb^{3+} content from 0 to 0.3. The average lifetimes (τ) are calculated to be about 5.81, 5.37, 4.73, 3.82, 2.08, 1.38 μs and η_{ETE} are 6.2%, 12.4%, 22.8%, 37.7%, 66.1% and 77.5% for x=0.01, 0.04, 0.08, 0.16, 0.20 and 0.30, respectively. It is worth mentioning that η_{ETE} reaches as high as 77.5% for $Ba_2LaV_3O_{11}$: 0.30Yb^{3+} sample.

3.3.3 Energy transfer mechanism in $Ba_2LaV_3O_{11}$: Yb^{3+}

The above luminescent spectra and decay lifetimes have proved the occurrence of ET from $[VO_4]^{3-}$ to Yb^{3+} in Yb^{3+} doped $Ba_2LaV_3O_{11}$ host. In order to comprehensive understand the ET process and the mechanism from $[VO_4]^{3-}$ group to Yb^{3+}, the schematic energy levels of $[VO_4]^{3-}$ and Yb^{3+} with possible energy transfer pathway are demonstrated in Fig. 6. Under the excitation of near ultraviolet light, $[VO_4]^{3-}$ groups are excited as a result of electron transfer from O-2*p* valence band to V-3*d* conduction band, and the radiative relaxation of the excited state to ground state could emit a green photon or transfer its energy to the nearby Yb^{3+} ions through ET process. As shown in the scheme, the ET from the $[VO_4]^{3-}$ to the Yb^{3+} has two possible routes: □ Cooperative ET: The energy of $[VO_4]^{3-}$ from $^3T_2$ / $^3T_1$ - $^1A_1$ transition is approximately twice as high as the energy difference between the $^2F_{7/2}$ and $^2F_{5/2}$ levels of Yb^{3+} and Yb^{3+} has no other levels up to UV region, thus the energy of $[VO_4]^{3-}$ is simultaneously transferred to two nearby Yb^{3+} ions emitting two NIR photons with a wavelength around 1000 nm. □ Single-photon ET: The excited state of $[VO_4]^{3-}$ group could split into two levels $^1T_{1,2}$ and $^3T_{1,2}$, and the energy of higher excited states is close to that of O^{2-} - Yb^{3+} charge transfer state (CTS).[18] With the help of multi phonons, the excited $[VO_4]^{3-}$ state can transfer its energy to CTS of Yb^{3+}, then Yb^{3+} undergo fast intra-ion thermal relaxation down to the excited $^2F_{5/2}$ state companied with energy loss, resulting a single NIR photon for each UV photon excitation. For the mentioned pathway, the former could convert one UV photon into two NIR photons (called QC), but the latter process is a one-to-one conversion process. However, both two processes are significant for application in enhancing efficiency of silicon-based solar cells by converting the inefficient UV photon for Si-based solar cell to available NIR photon at around 1000 nm where the Si solar cell exhibits the most efficient spectral response. According to previous theoretical calculation, the quantum yield (QY) is over 100% and reach about 200% in the former QC process, but almost all measured QY in the samples with so called "QC" are far below 100%,[34] which is due to the possible reasons: different detectors for Vis and NIR emission measurement; the direct ET from the excited $[VO_4]^{3-}$ state to CTS of Yb^{3+}. Fortunately, ET from $[VO_4]^{3-}$ to Yb^{3+} is sure to be occurred, NIR emission peaked at 977 and 1004 nm is available and offers the ability to improve the spectral response of the c-Si solar cells to short-wavelength sunlight.

According to previous results, the mechanism of the ET from VO_4^{3-} to Yb^{3+} in $Ba_2LaV_3O_{11}$: Yb^{3+} sample could be judged in light of the dependence of the energy transfer rate (W, related to reciprocal of the decay time of the sensitizer τ^{-1}) on Yb^{3+} ion concentration (x). For single-photon ET process, the host transfers its energy to sole Yb^{3+} ion. The energy transfer rate ($W_{S\text{-}ET}$) from a donor (VO_4^{3-}) to an acceptor (Yb^{3+}) can be written as $W_{S\text{-}ET} = A'x$, A is the sum of distance function multiply by the radiative decay rate and x is Yb^{3+} concentration. While the donor (VO_4^{3-}) synchronously transfers its energy to two acceptors (Yb^{3+}) for CET process, the relationship between energy transfer rate (W_{CET}) and Yb^{3+} doping concentration (x) is $W_{CET} = Ax^2$.[35, 36]

According to the lifetime values in Table 1, the ET rate ($W_{\text{Host-Yb}}$) can be expressed as follows: [35]

$$W_{\text{Host-Yb}} = \frac{1}{\tau_x} - \frac{1}{\tau_0} \tag{5}$$

Here $1/\tau_x$ means the total transfer rate when the Yb^{3+} content is x, and $1/\tau_0$ is the transfer rate when ET is inexistent (x=0). The double logarithmic plot of ET rates (W) versus Yb^{3+} doping concentration (x) is shown in Fig. 7. As discussed above, when the concentration of Yb^{3+} ions changes from 0.01 to 0.08, the slope n_1 value is about 1 indicating that the single-photon ET is dominant; while when x further increases to 0.30, the slope n_2 value is the calculated to be 2, displaying that the ET is mainly by the CET process as the content of Yb^{3+} in the range of 0.08-0.30.[36] On the basis of the above analysis, it indicates that the ET process from $[VO_4]^{3-}$ ions to Yb^{3+} ions dominated by the single-photon ET when the Yb^{3+} concentration is below 0.08; whereas, the CET process occurs and its possibility gradually rises with the increase of the Yb^{3+} concentration, when the Yb^{3+} ion concentration (x) exceeds 0.08 the CET process dominated the ET. Unfortunately, the proportion of the two processes can't be determined and the theoretical quantum yield cannot be calculated. However, the theoretical quantum yields (η_{TQY}, defined as the ratio of the number of photons emitted to the number of absorbed photons) of the samples doped with high concentration (x>0.08), in which the ET occurs only by the cooperative process, can be estimated as:[36]

$$\eta_{\text{TQY}} = \eta_{\text{Host}}(1-\eta_{\text{ETE}}) + 2\eta_{\text{Yb}}\eta_{\text{ETE}} \tag{6}$$

where η_{Host} and η_{Yb} are the internal quantum efficiencies of host and Yb^{3+}, respectively. Here, it is usually assumed that all the excited Yb^{3+} ions and the residual excited $[VO_4]^{3-}$ ions decay radiatively by ignoring the non-radiative energy loss, *i.e.*, $\eta_{\text{Host}}=\eta_{\text{Yb}}=1$. Therefore, the upper limit of the theoretical total QY is estimated to be about 137.7%, 166.1% and 177.5% for x= 0.16, 0.20, 0.30 according to *Eq.*(6). Therefore, the highest QY in the present samples has been found to be 177.5%, which indicates that 77.5% energy absorbed by host is transferred to $^2F_{5/2}$ level of Yb^{3+} ions to achieve the NIR emission and the energy transfer from host to Yb^{3+} is extremely efficient.

For clearly showing the applicability of present sample in Si-based solar cell, the PLE and PL spectra of $Ba_2LaV_3O_{11}$: $0.16Yb^{3+}$ phosphor with optimal composition, the AM 1.5G solar spectrum and the spectral response of c-Si solar cells are shown Fig. 8 with a comparable way. It is clear that the most efficiently spectral absorption of c-Si solar cells is 900-1100 nm NIR region where photons energy close to the silicon band gap ($E_g \approx 1.12$ eV, 1100 nm), but the UV-Vis light with much higher energy than that of band gap dominates the incident solar spectrum. $Ba_2LaV_3O_{11}$ could absorb the UV-Vis light with wavelength below 400 nm and emit broadband visible light in 400-700 nm (blue line), while Yb^{3+}-doped $Ba_2LaV_3O_{11}$ NIR DC phosphors offer the strong absorption in UV region (240-400 nm, purple line) and give intense NIR emission (900-1100 nm, red line) in the optimal response region of c-Si solar cells. Therefore, $Ba_2LaV_3O_{11}$ and Yb^{3+}-doped $Ba_2LaV_3O_{11}$ down-conversion phosphors have great potential applications in enhancing the efficiency of silicon-based solar cells.

4. Conclusions

In summary, a class of $Ba_2LaV_3O_{11}$: Yb^{3+} NIR down-conversion phosphor *are* synthesized by sol-gel reaction. The host $Ba_2LaV_3O_{11}$ shows broad PLE band from 240 to 395 nm associated with CTB (CT band) of $[VO_4]^{3-}$ group, and intense broad band yellow-green emission ranging from 400 to 700 nm centered at 502 nm. The efficient NIR emission of Yb^{3+}-doped $Ba_2LaV_3O_{11}$ samples from 900 to1100 nm match well with the optimal spectral response of the c-Si solar cells. The energy transfer plays a critical role in the Yb^{3+}-doped $Ba_2LaV_3O_{11}$ phosphors, and the decreasing lifetimes of host emission with increasing Yb^{3+} are measured to prove the occurrence of ET from host to Yb^{3+}. Based on the analysis of relationship between the energy transfer rate and Yb^{3+} content, the possible energy transfer processes and NIR emission mechanism in $Ba_2LaV_3O_{11}$: Yb^{3+} phosphors are proposed. It illuminates that the ET process from $[VO_4]^{3-}$ group to Yb^{3+} ions is dominated by single-photon ET process when the Yb^{3+} concentration is below 0.08; whereas the ET mainly occurs through the CET process when dosage concentration (x) exceeds 0.08 and the estimated highest theoretical quantum yield reaches 177.5% at x = 0.30. Results demonstrate that the present $Ba_2LaV_3O_{11}$ and $Ba_2LaV_3O_{11}$: Yb^{3+} down-conversion phosphors could be used as solar spectral converters, which could make full use of the sunlight and enhance the efficiency of silicon-based solar cells.

Acknowledgements

This work was supported by the high-level talent project of Northwest University, National

Natural Science Foundation of China (No. 11274251), Ph.D. Programs Foundation of Ministry of Education of China (20136101110017), Technology Foundation for Selected Overseas Chinese Scholar, Ministry of Personnel of China (excellent), Natural Science Foundation of Shaanxi Province (No.2014JM1004) and Foundation of Key Laboratory of Photoelectric Technology in Shaanxi Province (12JS094).

References

1 A. Solodovnyk, K. Forberich, E. Stern, J. Krc, M. Topic, B. Lipovsek and C. J. Brabec, *Opt. Mater. Express*, 2015, **5**, 1296-1305.

2 A.J. Nozik and J. R. Miller, *Chem. Rev.*, 2010, **110**, 6443-6445.

3 Z. He, C. Zhong, S. Su, M. Xu, H. Wu and Y. Cao, *Nat. Photonics*, 2012, **6**, 591-597.

4 J. Zhao, C. Guo and T. Li, *RSC Adv.*, 2015, **5**, 28299-28304.

5 W. Shockley and H. J. Queisser, *J. Appl. Phys.* 1961, **32**, 510-519.

6 X. Huang, S. Han, W. Huang and X. Liu, *Chem. Soc. Rev.*, 2013, **42**, 173-201.

7 Y. Chen, J. Wang, C. Liu, J. Tang, X. Kuang, M. Wu and Q. Su, *Opt. Express*, 2013, **21**, 3161-3169.

8 B.M. van der Ende, L. Aarts and A. Meijerink, *Adv. Mater.*, 2009, **21**, 3073-3077.

9 H. Wang, S. Ye, T. Liu, Li Song, R. Hua and D. Wang, *J. Rare Earths*, 2015, **33**, 524-528.

10 Y. Xu, F. Huang, B. Fan, C. Lin, S. Dai, L. Chen, Q. Nie, H. Ma and X. Zhang, *Opt. Lett.*, 2014, **39**, 2225-2228.

11 X. Zhou, Y. Wang, X. Zhao, L. Li, Z. Wang and Q. Li, *J. Am. Ceram. Soc.*, 2014, **97**, 179-184.

12 J. Sun, Y. Sun, C. Cao, Z. Xia and H. Du, *Appl. Phys. B*, 2013, **111**, 367-371.

13 Z. Fang, R. Cao, F. Zhang, Z. Ma, G. Dong and J. Qiu, *J. Mater. Chem. C*, 2014, **2**, 2204-2211.

14 T. Liu, G. Zhang, X. Qiao, J. Wang, H. J. Seo, D. Tsai, and R. S. Liu, *Inorg. Chem.*, 2013, **52**, 7352-7357.

15 Z. Liu, J. Li, L. Yang, Q. Chen, Y. Chu and N. Dai, *Sol. Energy Mat. Sol. C.*, 2014, **122**, 46-50.

16 R. Zhou, X. Wei, S. Huang, Y. Chen and M. Yin, *J. Alloy Compd.*, 2012, 537, 123-126.

17 X. Liu, L. Li, H. M. Noh, B. K. Moon, B. C. Choib and J. H. Jeong, *Dalton Trans.*, 2014, **43**, 8814-8825.

18 X. Wei, S. Huang, Y. Chen, C. Guo and M. Yin, *J. Appl. Phys.*, 2010, **107**, 103107.

19 Y. Lu, Y. Li, L. Qin, Y. Huang, C. Qin, T. Tsuboi and W. Huang, *Mater. Res. Bull.*, 2015, **64**, 425-431.

20 V. Milmanm, B. Winkler, J. A. White, J. Pickard, M. C. Payne, E. V. Akhmatskaya and R. H. Nobes, *Int. J. Quantum Chem.*, 2000, **77**, 895-910.

21 G. Kresse and J. Hafner, *Phys. Rev. B.*, 1993, **47**, 558-561.

22 J. P. Perdew, K. Burke and M. Ernzerhof, *Phys. Rev. Lett.*, 1996, **77**, 3865-3868.

23 J. Huang, Q. Gu and A.W. Sleight, *J. Solid State Chem.*, 1994, **110**, 226-233.

24 J. Boje and H. K. Miiller-Buschbaum, *Z. anorg. allg. Chcrn.*,1993, **619** , 525-528.

25 Y. Q. Li, N. Hirosaki, R. J. Xie, T. Takeka and M. Mitpmo, *J. Solid State Chem.*, 2009, **182**, 301-311.

26 P. Kubelka and F. Munk. *Z. Tech. Phys. (Leipzig)*, 1931, **12**, 593-601.

27 D. Deng, H. Yu and S. Xu, *J. Mater. Chem. C*, 2013, **1**, 3194-3199.

28 Z. Jiang, Y. Wang, Z. Ci and H. Jiao, *J. Electrochem. Soc.,* 2009, **156**, J317-J320.

29 J. Zhou, F. Huang, J. Xu, H. Chen and Y. Wang, *J. Mater. Chem. C*, 2015, **3**, 3023-3028.

30 E. Pavitra, G. S. R Raju, J. Y. Park, L. Wang and B. K. Moon, *Sci. Rep.*, 2015, **5**, 10296.

31 Y. Li, J. Wang, W. Zhou, G. Zhang, Y. Chen and Q. Su, *Appl. Phys. Express.*, 2013, **6**, 082301.

32 Y. Jia, H. Qiao, Y. Zheng, N. Guo and H. You, *Phys. Chem. Chem. Phys.*, 2012, **14**, 3537-3542.

33 P. Vergeer, T. Vlugt, M. Kox, M. den Hertog, J. van der Eerden and A. Meijerink, *Phys. Rev. B*, 2005, **71**, 014119.

34 J. Ueda and S. Tanabe, *J. Appl. Phys.*, 2009, **106**, 043101.

35 J. Li, L. Chen, Z. Hao, X. Zhang, L. Zhang, Y. Luo and J. Zhang., *Inorg. Chem.*, 2015, **54**, 4806-4810.

36 G. Xiang, J. Zhang, Z. Hao, X. Zhang, G. Pan, Y. Luo, S. Lv and H. Zhao, *Phys. Chem. Chem. Phys.*, 2014, **16**, 9289-9293.

Figure captions:

Fig. 1 (**a**) XRD patterns of phosphors $Ba_2LaV_3O_{11}$: xYb^{3+} (x = 0, 0.01, 0.08, 0.16, 0.20, 0.30) with the standard profile of $Ba_2BiV_3O_{11}$ (JCPDS 81-1778); (**b**) Enlarged (021) peak in various XRD patterns; (**c**) The crystal structure of $Ba_2LaV_3O_{11}$.

Fig. 2 (a) The calculated energy band structure of $Ba_2LaV_3O_{11}$; **(b)** DOS of $Ba_2LaV_3O_{11}$ (Fermi level at 0 energy).

Fig. 3 (a) UV-Vis diffuse reflectance spectrum (DRS) and **(b)** $(\alpha h\upsilon)^2$-$h\upsilon$ curve of $Ba_2LaV_3O_{11}$ sample.

Fig. 4 PLE (λ_{em}=502 nm) and PL (λ_{ex}=338 nm) spectra of $Ba_2LaV_3O_{11}$ with their Gaussian components **(a)** and schematic energy level for excitation and emission processes in the $(VO_4)^{3-}$ tetrahedron **(b)**.

Fig. 5 (**a**) PLE spectra of $Ba_2LaV_3O_{11}$ (λ_{em} = 502 nm) and $Ba_2LaV_3O_{11}$: 0.16Yb^{3+} (λ_{em} = 1004 nm), (**b**) PL spectra of $Ba_2LaV_3O_{11}$: xYb^{3+} (x = 0, 0.01, 0.08, 0.16, 0.20, 0.30) in visible / NIR (λ_{ex} = 338 nm) and (**c**) Vis/NIR integrated intensity and (**d**) decay lifetime of $[VO_4]^{3-}$ emission depends on the Yb^{3+} concentration x under 338 nm excitation.

Fig. 6 Schematic energy level diagram and the possible energy transfer process for VO_4^{3-} and Yb^{3+} in $Ba_2LaV_3O_{11}$.

Fig. 7 Plot (*log-log*) of the energy transfer rate ($W_{\text{Host-Yb}}$) *vs.* Yb^{3+} concentration (x) in $Ba_2LaV_3O_{11}$: xYb^{3+} (x = 0.01, 0.04, 0.08, 0.16, 0.20, 0.30).

Fig. 8 AM 1.5G solar spectrum (black line) and spectral response of c-Si solar cells (green line). PLE (λ_{em} = 1004 nm) and PL (λ_{em} = 338 nm) spectra of $Ba_2LaV_3O_{11}$: 0.16Yb^{3+} phosphor.

Figures:

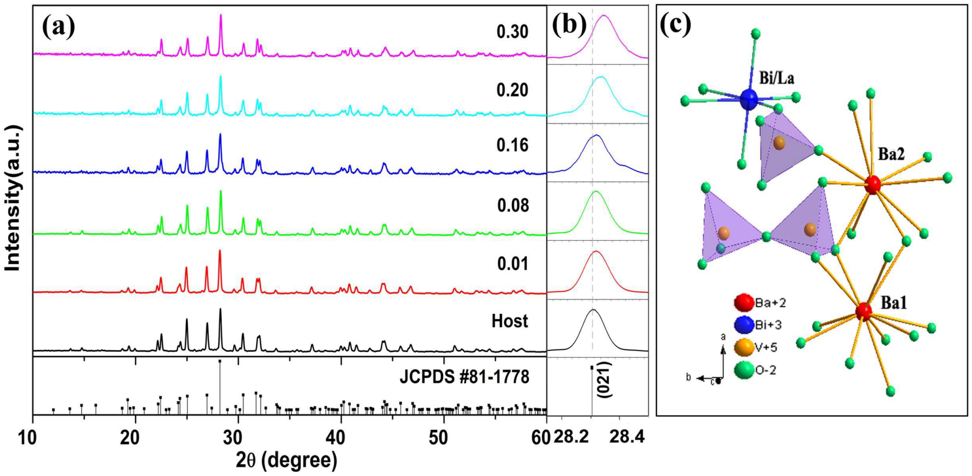

Fig. 1 (**a**) XRD patterns of phosphors $Ba_2LaV_3O_{11}$: $x$$Yb^{3+}$ (x = 0, 0.01, 0.08, 0.16, 0.20, 0.30) with the standard profile of $Ba_2BiV_3O_{11}$ (JCPDS 81-1778); (**b**) Enlarged (021) peak in various XRD patterns; (**c**) The crystal structure of $Ba_2LaV_3O_{11}$.

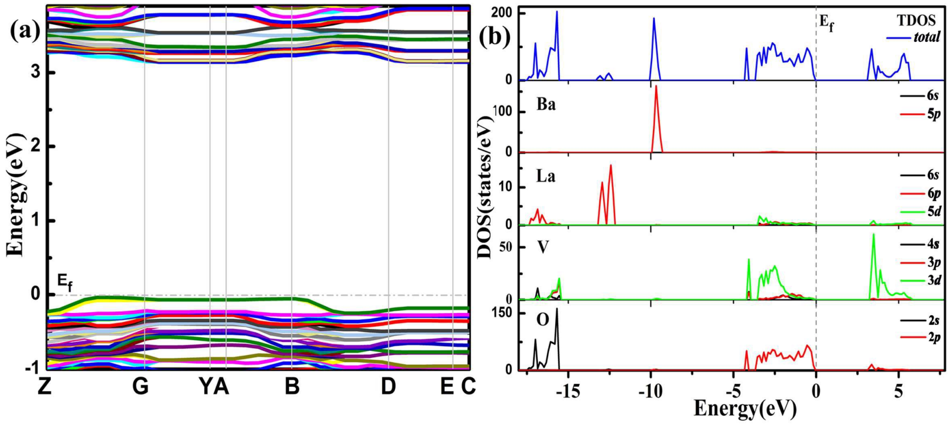

Fig. 2 (a) The calculated energy band structure of $Ba_2LaV_3O_{11}$; **(b)** DOS of $Ba_2LaV_3O_{11}$ (Fermi level at 0 energy).

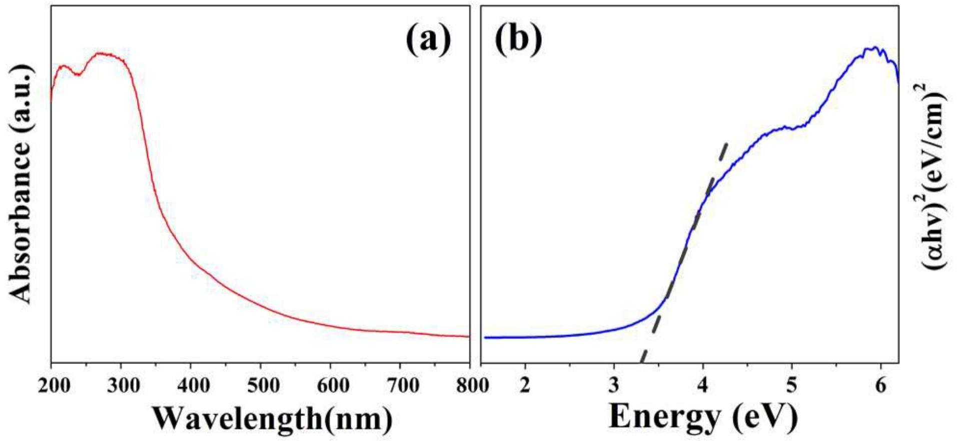

Fig. 3 **(a)** UV-Vis diffuse reflectance spectrum (DRS) and **(b)** $(\alpha h\upsilon)^2$-$h\upsilon$ curve of $Ba_2LaV_3O_{11}$ sample.

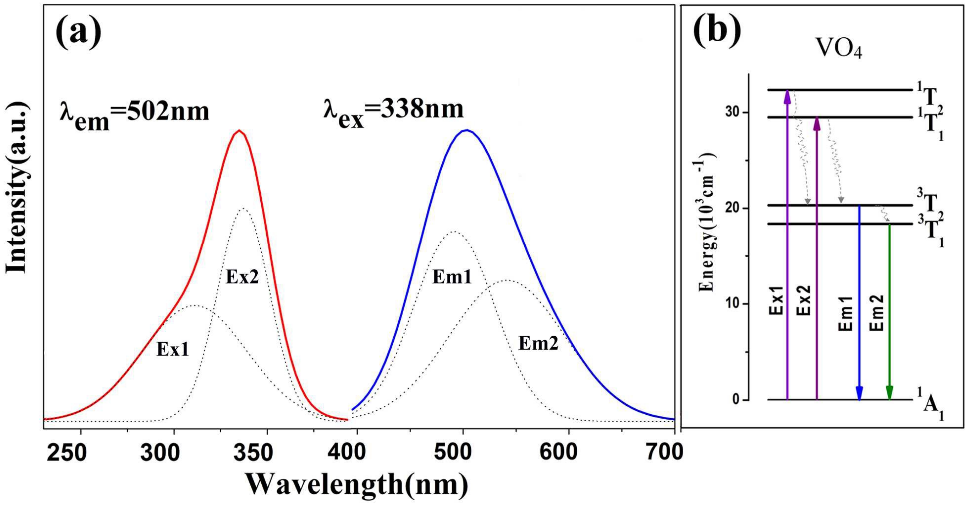

Fig. 4 PLE (λ_{em}=502 nm) and PL (λ_{ex}=338 nm) spectra of $Ba_2LaV_3O_{11}$ with their Gaussian components **(a)** and schematic energy level for excitation and emission processes in the $(VO_4)^{3-}$ tetrahedron **(b)**.

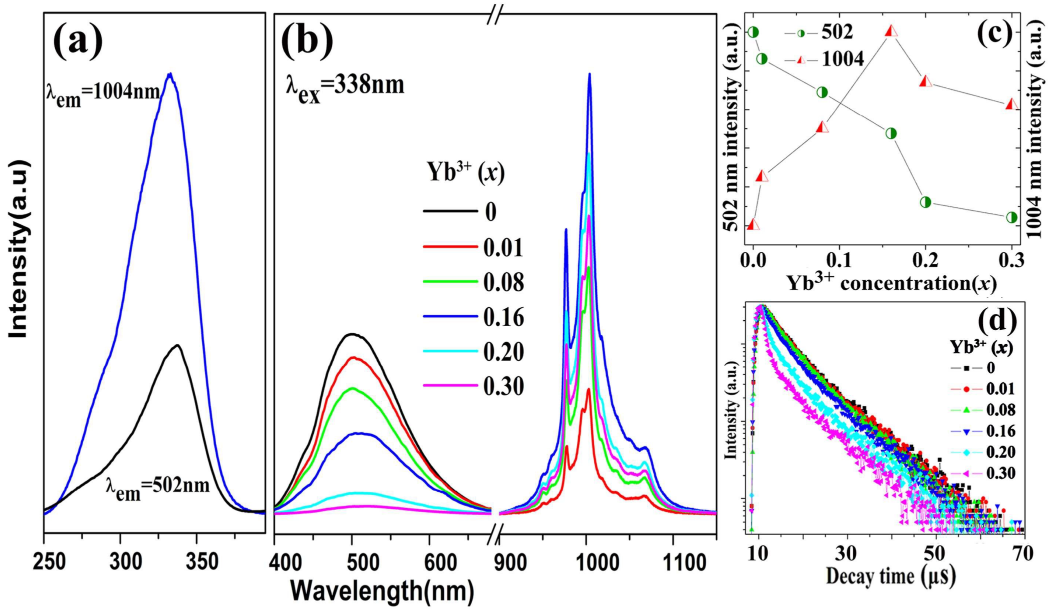

Fig. 5 (**a**) PLE spectra of $Ba_2LaV_3O_{11}$ (λ_{em} = 502 nm) and $Ba_2LaV_3O_{11}$: $0.16Yb^{3+}$ (λ_{em} = 1004 nm), (**b**) PL spectra of $Ba_2LaV_3O_{11}$: xYb^{3+} (x = 0, 0.01, 0.08, 0.16, 0.20, 0.30) in visible / NIR (λ_{ex} = 338 nm) and (**c**) Vis/NIR integrated intensity and (**d**) decay lifetime of $[VO_4]^{3-}$ emission depends on the Yb^{3+} concentration x under 338 nm excitation.

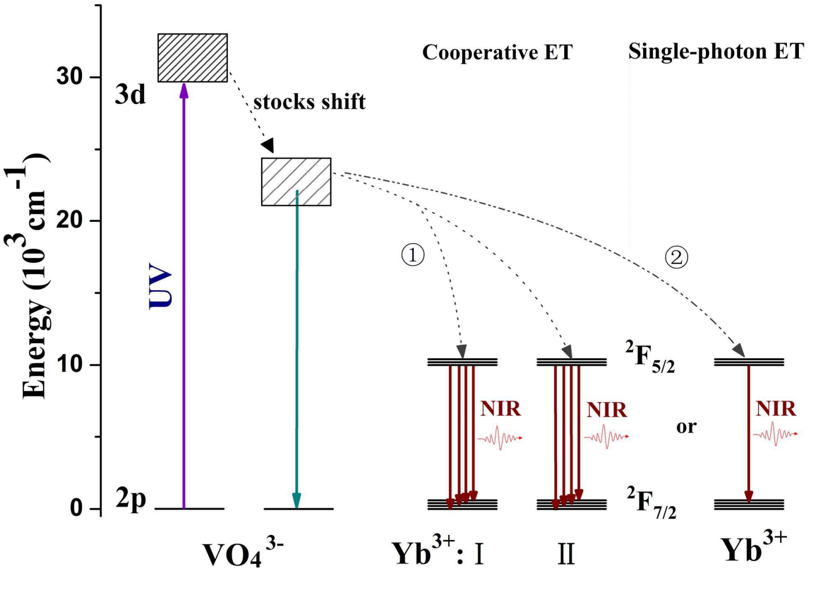

Fig. 6 Schematic energy level diagram and the possible energy transfer process for VO_4^{3-} and Yb^{3+} in $Ba_2LaV_3O_{11}$.

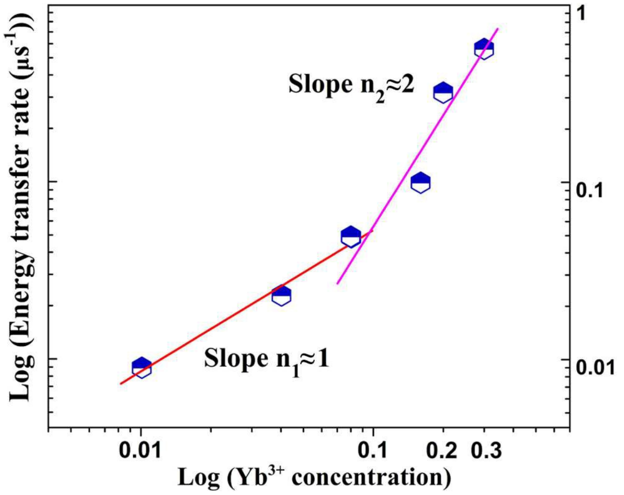

Fig. 7 Plot (*log-log*) of the energy transfer rate ($W_{\text{Host-Yb}}$) *vs.* Yb^{3+} concentration (x) in $Ba_2LaV_3O_{11}$: $x$$Yb^{3+}$ (x = 0.01, 0.04, 0.08, 0.16, 0.20, 0.30).

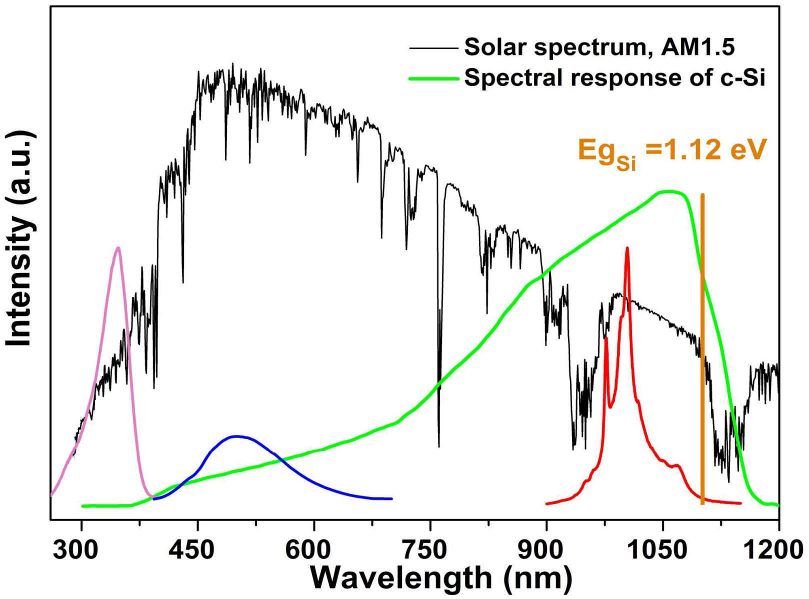

Fig. 8 AM 1.5G solar spectrum (black line) and spectral response of c-Si solar cells (green line). PLE (λ_{em} = 1004 nm) and PL (λ_{em} = 338 nm) spectra of $Ba_2LaV_3O_{11}$: 0.16Yb^{3+} phosphor.

Table 1

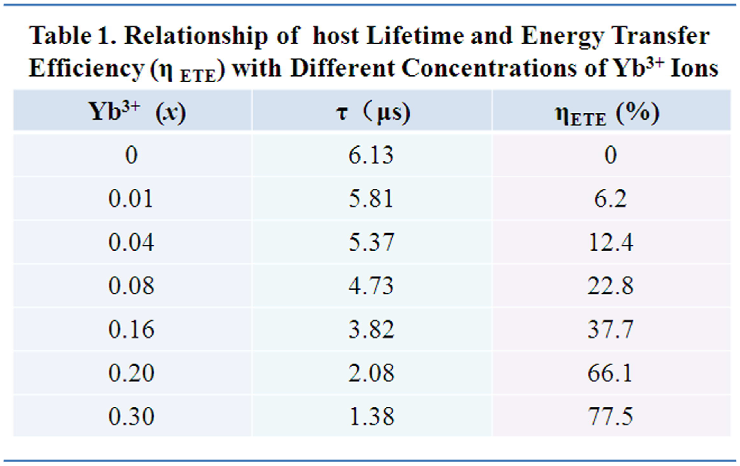

Table 1. Relationship of host Lifetime and Energy Transfer Efficiency (η_{ETE}) with Different Concentrations of Yb^{3+} Ions

Yb^{3+} (x)	τ (μs)	η_{ETE} (%)
0	6.13	0
0.01	5.81	6.2
0.04	5.37	12.4
0.08	4.73	22.8
0.16	3.82	37.7
0.20	2.08	66.1
0.30	1.38	77.5